SWIFT OBSERVATIONS OF THE X-RAY–BRIGHT GRB 050315

S. Vaughan,[1] M. R. Goad,[1] A. P. Beardmore,[1] P. T. O'Brien,[1] J. P. Osborne,[1] K. L. Page,[1] S. D. Barthelmy,[2]
D. N. Burrows,[3] S. Campana,[4] J. K. Cannizzo,[2,5] M. Capalbi,[6] G. Chincarini,[4,7] J. R. Cummings,[2,8]
G. Cusumano,[9] P. Giommi,[6] O. Godet,[1] J. E. Hill,[2,10] S. Kobayashi,[3] P. Kumar,[11] V. La Parola,[9]
A. Levan,[1] V. Mangano,[9] P. Mészáros,[3] A. Moretti,[4] D. C. Morris,[3] J. A. Nousek,[3]
C. Pagani,[3,4] D. M. Palmer,[12] J. L. Racusin,[3] P. Romano,[4] G. Tagliaferri,[4]
B. Zhang,[13] and N. Gehrels[2]
Received 2005 August 4; accepted 2005 October 21

ABSTRACT

This paper discusses *Swift* observations of the γ-ray burst GRB 050315 ($z = 1.949$) from 80 s to 10 days after the onset of the burst. The X-ray light curve displayed a steep early decay (t^{-5}) for $\sim$200 s and several breaks. However, both the prompt hard X-ray/γ-ray emission (observed by the BAT) and the first $\sim$300 s of X-ray emission (observed by the XRT) can be explained by exponential decays, with similar decay constants. Extrapolating the BAT light curve into the XRT band suggests that the rapidly decaying, early X-ray emission was simply a continuation of the fading prompt emission; this strong similarity between the prompt γ-ray and early X-ray emission may be related to the simple temporal and spectral character of this X-ray–rich GRB. The prompt (BAT) spectrum was steep down to $\sim$15 keV and appeared to continue through the XRT bandpass, implying a low peak energy, inconsistent with the Amati relation. Following the initial steep decline, the X-ray afterglow did not fade for $\sim$1.2 × 10⁴ s, after which time it decayed with a temporal index of $\alpha \approx 0.7$, followed by a second break at $\sim$2.5 × 10⁵ s to a slope of $\alpha \sim 2$. The apparent "plateau" in the X-ray light curve, after the early rapid decay, makes this one of the most extreme examples of the steep-flat-steep X-ray light curves revealed by *Swift*. If the second afterglow break is identified with a jet break, then the jet opening angle was $\theta_0 \sim 5°$, implying $E_\gamma \gtrsim 10^{50}$ ergs.

Subject headings: gamma rays: bursts — X-rays: individual (GRB 050315)

Online material: color figures

1. INTRODUCTION

The *Swift* γ-ray burst explorer (Gehrels et al. 2004) was successfully launched on 2004 November 20 and is now routinely taking observations of gamma-ray bursts (GRBs) and their afterglows in the crucial minutes to hours after the burst, delivering insights into the nature of the prompt emission and early afterglow phase. New bursts are detected by the Burst Alert Telescope (BAT; Barthelmy 2004; Barthelmy et al. 2005a), a coded-mask imager with a with a 1.4 sr field of view (half-coded) sensitive to 15–350 keV energies, with imaging capability over the 15–150 keV

range. The spacecraft is able to slew autonomously to the burst position within a few tens of seconds. Once on-target, data are collected with two co-aligned narrow-field instruments: the X-ray Telescope (XRT; Burrows et al. 2004, 2005a) and the Ultraviolet/Optical Telescope (UVOT; Roming et al. 2005).

In this paper, we report on the *Swift* observations of GRB 050315. The BAT triggered and located GRB 050315 onboard at 2005 March 15 20:59:42 UT (Parsons et al. 2005). The spacecraft automatically slewed to the burst location, and the XRT and UVOT began observations starting ≈80 s after the BAT trigger, one of the earliest XRT observations yet made. The XRT observation continued to detect the source for $\sim$10 days, providing one of the best-sampled X-ray light curves of a GRB afterglow to date. At the time of writing there are $\sim$20 *Swift* bursts with known redshifts; besides GRB 050315, four of these have XRT detections out to $\sim$10 days postburst: GRB 050319 (Cusumano et al. 2006), GRB 050525a (Blustin et al. 2006), GRB 050603 (Nousek et al. 2005), and GRB 050401 (De Pasquale et al. 2006). The spectroscopic redshift $z = 1.949$ (Kelson & Berger 2005b) places GRB 050315 below the $z \approx 2.8$ mean redshift for *Swift* bursts estimated by Jakobsson et al. (2006).

In this paper we present a detailed analysis of the XRT data of GRB 050315 from the first minutes to several days after the burst. The plan for the paper is as follows. Section 2 reviews the basic details of the *Swift* observations from each instrument. Then § 3 presents a detailed analysis of the XRT images, light curve, and spectrum. Due to the very high initial count rate for the source, and the mode of the XRT camera during the observation, the early data suffered severely from pileup; this problem is also discussed in § 3, along with a simple "work-around" solution. Section 4 presents a comparison of the XRT and BAT data for the first few

[1] Department of Physics and Astronomy, University of Leicester, Leicester LE1 7RH, UK.
[2] NASA Goddard Space Flight Center, Greenbelt, MD 20771.
[3] Department of Astronomy and Astrophysics, Pennsylvania State University, 525 Davey Lab, University Park, PA 16802.
[4] INAF–Osservatorio Astronomico di Brera, Via Bianchi 46, 23807 Merate, Italy.
[5] Joint Center for Astrophysics, University of Maryland, Baltimore County, Baltimore, MD 21250.
[6] ASI Science Data Center, Via Galileo Galilei, I-00044 Frascati (Rome), Italy.
[7] Universitá degli studi di Milano-Bicocca, Dipartimento di Fisica, Piazza delle Scienze 3, I-20126 Milan, Italy.
[8] National Research Council, 2101 Constitution Avenue, NW, Washington, DC 20418.
[9] INAF–Istituto di Astrofisica Spaziale e Fisica Cosmica Sezione di Palermo, Via Ugo La Malfa 153, I-90146 Palermo, Italy.
[10] Universities Space Research Association, 10211 Wincopin Circle, Suite 500, Columbia, MD, 21044-3432.
[11] Department of Astronomy, University of Texas, Austin, TX 78712.
[12] Los Alamos National Laboratory, P.O. Box 1663, Los Alamos, NM 87545.
[13] Department of Physics, University of Nevada, Box 454002, Las Vegas, NV 89154-4002.

hundred seconds after the BAT trigger. Finally, § 5 summarizes the main results and gives a brief discussion of some of the implications of this work. For the purpose of calculating luminosities, the cosmological parameters were taken to be those of the *Wilkinson Microwave Anisotropy Probe* (*WMAP*) standard cosmology, namely, $H_0 = 70$ km s^{-1} Mpc^{-1} with $\Omega_m = 0.27$ and $\Omega_\Lambda = 0.73$.

2. OBSERVATIONS AND BASIC DATA REDUCTION

2.1. *BAT Observations*

The BAT event data were analyzed using the standard BAT analysis software (Build 20) as described in the *Swift* BAT Ground Analysis Software Manual (Krimm et al. 2004). Slew data were processed with the corrected ray-tracing procedure for slew data,[14] and light curves and spectra were extracted.

Figure 1 shows the BAT light curve, which comprises two overlapping fast rise, exponential decay (FRED)-like peaks, and a possible precursor starting ~60 s before the trigger and continuing up to the main peak. The first peak rose over approximately 10 s followed by a gradual decline, interrupted by a second peak at $T_0 + 22$ s. The burst duration including the precursor was $T_{90} = 96$ s. The BAT light curve from T_0 was binned such that each bin had a signal-to-noise ratio greater than 3 (i.e., $I/\sigma_I > 3$) and was fitted with an exponential curve, $\exp(-t/t_e)$. Ignoring the period 20–30 s posttrigger, which was dominated by the second, shorter peak, the exponential curve gave a good fit ($\chi^2 = 35.39$ for 32 degrees of freedom [dof] and a rejection probability of $p = 0.69$) with a decay constant of $t_e = 24 \pm 2$ s. The hardness ratio time series, derived from four-band BAT light curves, clearly showed a softening of the burst spectrum with time.

The BAT spectra were extracted from the full time interval over which the burst was detected and also from intervals covering the 1 s peak, T_{50}, and T_{90}. The spectra were fitted over the 15–150 keV range using XSPEC, version 11.3 (Arnaud 1996). In all cases a simple power law provided a good fit, with no evidence for a spectral break within the available bandpass; fitting with sharply breaking power law or a Band function (Band et al. 1993) did not substantially improve the fit ($\Delta \chi^2 < 4$). For the four time intervals the photon indices [$N_{ph}(E) \propto E^{-\Gamma}$] were $\Gamma = 2.16 \pm 0.07$ (total), 2.3 ± 0.2 (1 s peak), 2.02 ± 0.07 (T_{50}), and 2.13 ± 0.07 (T_{90}). The 1 s peak flux was 2.2 ± 0.5 photons cm^{-2} s^{-1} in the 15–150 keV band (see also Sakamoto et al. 2005; Krimm et al. 2005), and the total burst fluence was $3.4 \pm 0.3 \times 10^{-6}$ ergs cm^{-2} (also 15–150 keV).

If only a single photon index is measured, it is difficult to constrain the bend or peak energy of a GRB spectrum. In order to constrain the bend energy for GRB 050315, a Band function was fitted to the BAT data from the full time interval assuming $\alpha = -1.3$ (the mean from the Amati et al. 2002 sample) but with all other parameters free. The bend energy E_0 was constrained to lie below 43 keV (in the observed frame) at the 90% confidence limit (CL). This corresponds to an upper limit on the peak energy $E_{peak} = E_0(2 + \alpha)$ of 30 keV (90% CL) or 36 keV (99% CL). Assuming $\alpha = -1.88$ (the steepest from the Amati et al. 2002 sample) gave an upper limit of $E_{peak} < 31$ keV (90% CL) or 40 keV (99% CL), indicating that the limit on E_{peak} is quite robust to the assumed value for α.

2.2. *XRT Observations*

At the time of the BAT trigger, the XRT was in manual state, making preplanned observations of GRB 050306 in photon counting (PC) mode, which meant that after the slew to GRB 050315
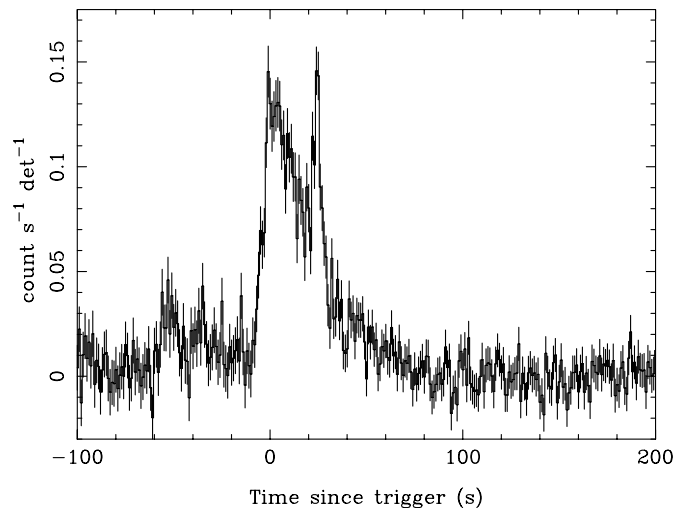
Fig. 1.—BAT light curve of GRB 050315 in 1 s bins.

the standard set of XRT observations was not implemented, and thus the early image mode (IM) snapshot, normally taken once the spacecraft has settled, was not taken in this instance. See Hill et al. (2004) and Burrows et al. (2004) for a description of the XRT readout modes. The absence of IM data immediately following the slew prevented an early XRT position determination. Ground analysis of the early PC data identified a new, rapidly fading source at (J2000.0) R.A. = $20^h25^m54^s$, decl. = $-42°36'0''.2$ (Morris et al. 2005).

There was also 0.9 ks of exposure taken in windowed timing (WT) mode, during orbits when the XRT camera was rapidly switching between PC and WT modes due to high background. For most of these orbits there are not enough source counts for a robust detection, and so these data were not used in the subsequent analysis.

The XRT data were processed by the *Swift* Data Center at NASA/Goddard Space Flight Center (GSFC) to level 1 data products (calibrated, quality flagged event lists). These were further processed with the processing pipeline xrtpipeline, version 0.8.8, into level 2 data products. The CCD operating temperature was between $-54.5°$C and $-61.5°$C, almost $50°$C warmer than the original design temperature, which led to a large number of hot and flickering pixels. These were flagged using the xrthotpix tool during the pipeline processing. High optical background light (e.g., due to the bright Earth limb) dominates XRT spectra at low energies; these events were filtered out in the pipeline processing, and subsequently all events with energies <0.2 keV were ignored.

The first useful XRT data taken during the first orbit were four frames (10 s) during the "settling" phase (when the pointing was within 10' but not stable), starting at $T_0 + 73.5$ s. During the first CCD frame the source is spread over the image, but it is relatively stable in the later three frames. These frames (7.5 s exposure from 76 to 83.5 s postburst) were included in the XRT data analysis. The pointed phase PC observation (once the spacecraft pointing was stable) began in earnest at $T_0 + 86$ s. Following this, GRB 050315 was observed during a further 100 orbits of *Swift*.

2.3. *UVOT Observations*

In a 100 s exposure taken approximately 90 s after the trigger, UVOT detected no new source down to a 5 σ limiting magnitude of 18.5 in the *V* band (Rosen et al. 2005).

2.4. *Other Observations*

Ground-based *r*-band observations with the low-dispersion survey spectrograph (LDSS) instrument on Magellan-Clay detected a new source within the XRT error circle (Kelson & Berger 2005a). A 20 minute spectrum of the afterglow identified Al III $\lambda\lambda$1854.7, 1862.8 and Si II λ1808.0 absorption lines at a redshift $z = 1.949$ (Kelson & Berger 2005b). Using the fluence of 3.4×10^{-6} ergs cm^{-2}, this implies an isotropic equivalent γ-ray energy of $E_{\rm iso} = 3.3 \times 10^{52}$ ergs (over 15–150 keV in the observer frame).

Soderberg & Frail (2005) reported a Very Large Array (VLA) radio counterpart at 8.5 GHz at the location of the burst. Bersier et al. (2005) reported an *I*-band magnitude of 20.7, 0.48 days after the burst trigger. Cobb & Bailyn (2005), on behalf of the SMARTS (Small and Moderate Aperture Research Telescope System) consortium, found an *R*-band decay with a slope of -0.57 (over 11.6–35.6 hr after the burst).

3. XRT ANALYSIS

3.1. *Pileup Estimation*

If more than one X-ray photon is collected in a given detector pixel in a single frame, the charges produced by the two separate events are recorded as one. This effect is known as "pileup." This is only part of the full story, however. The charge produced by a cosmic X-ray may be spread over one or more pixels (monopixel or split-pixel events); the shape of the charge distribution determines the "grade" of the event (or "pattern" in the *XMM-Newton* nomenclature). Pileup also occurs when two X-rays are collected in neighboring pixels in one frame (i.e., the patterns overlap). Such an event might be recorded as one split-pixel event rather than two separate events, or it might be rejected entirely, as diagonal charge patterns are not produced directly by X-rays. The effects of pileup are an apparent loss of flux, particularly from the center of the point spread function (PSF), and a change in the grade distribution and energies of events at high input count rates.

Ballet (1999) presented a very thorough treatment of flux losses as a result of pileup. Equation (6) of that paper shows how the *observed* rate of monopixel events varies with the *true* rate of incoming X-rays as a function of the CCD properties and the PSF. In order to examine at what count rates pileup becomes significant for the XRT in PC mode, this function was computed numerically, using different input count rates, assuming the following instrumental parameters. The clean (not piled up) PSF was assumed to be a King profile (eq. [B1] of Ballet 1999) with parameters $r_c = 6''.49$ and $\beta/2 = 1.59$, as measured for the XRT at 1.49 keV[15] from ground calibration tests (Moretti et al. 2004). The probability that an X-ray event produces a CCD event with a charge pattern containing i pixels was $\alpha_i = 0.778, 0.195, 0.014,$ and 0.013 for $i = 1, 2, 3,$ and 4, respectively, as appropriate for the MOS CCD at 1.49 keV.

The probability that an incident X-ray photon produces a monopixel event is thus $\alpha_1 = 0.778$ in the limit of no pileup. See Ballet (1999) and Mukerjee et al. (2003) for more details. Using these numbers, and the CCD frame time of $\Delta T = 2.507$ s, the rate of monopixel events, with and without pileup, was computed as a function of input X-ray count rate. The results are shown in Table 1, where column (1) shows the total input X-ray count rate (Λ), column (2) shows the expected rate of monopixel events assuming no pileup ($= \alpha_1\Lambda$), column (3) shows the expected number of monopixel events after pileup (M_1), and column (4) shows the ratio of monopixel event count rates with and

[15] The mean photon energy for GRB 050315 was $\approx$1.57 keV.

TABLE 1
EFFECTIVE LOSSES DUE TO PILEUP

Input[a] (counts s^{-1}) (1)	No Pileup[b] (counts s^{-1}) (2)	Pileup[c] (counts s^{-1}) (3)	Efficiency[d] (4)
1.29×10^{-2}..........	1.00×10^{-2}	9.98×10^{-3}	0.998
1.29×10^{-1}..........	1.00×10^{-1}	9.78×10^{-2}	0.978
3.21×10^{-1}..........	2.50×10^{-1}	2.37×10^{-1}	0.947
6.43×10^{-1}..........	5.00×10^{-1}	4.49×10^{-1}	0.899
1.28......................	1.00	8.18×10^{-1}	0.818
3.21......................	2.50	1.63	0.652
6.43......................	5.00	2.53	0.507
1.29×10^{1}............	1.00×10^{1}	3.81	0.380
3.21×10^{1}............	2.50×10^{1}	6.37	0.255
1.29×10^{2}............	1.00×10^{2}	1.30×10^{1}	0.131

[a] Rate of incoming X-rays: Λ.
[b] "True" rate of monopixel events (excluding pileup): $\alpha_1\Lambda$.
[c] "Observed" rate of monopixel events (including pileup): M_1.
[d] Ratio of observed/true count rates: $\eta = M_1/\alpha_1\Lambda$.

without pileup ($\eta = M_1/\alpha_1\Lambda$). It was evident from this calculation that even at (observed monopixel event) count rates as low as <0.1 counts s^{-1} the losses are $\sim$1%, and by 1 count s^{-1} the expected flux loss is $\sim$20%.

3.2. *Image Analysis*

Figure 2 shows two images extracted from the first XRT data set (observation ID 00111063000, spanning the first 10 orbits of data) and plotted in detector coordinates. Figure 2*a* shows the image formed from monopixel (grade = 0) events with photon energies in the range 0.2–5 keV accumulated during the first 10 orbits. There are virtually no source photons at energies >5 keV, so only lower energy events were included in the analysis. Only single-pixel events were used, as these should be affected least by pileup. For comparison, Figure 2*b* shows the image formed from events in the same energy range, also from monopixel events, from only the first 60 s of exposure, when the source was brighter than >5 counts s^{-1}. The center of the second image is clearly deficient in counts due to pileup.

The effects of pileup were clearly illustrated by an examination of the X-ray image as a function of observed count rate. A preliminary light curve was accumulated from single-pixel, 0.2–5.0 keV events extracted from a circle of radius 25 pixels centered on the brightest pixel in the center of the image shown in Figure 2*a*. The time bin size was set to be 25 s (10 CCD frames). This light curve was used to define three time intervals: (1) "bright" time, when the observed source count rate was >5 counts s^{-1}; (2) "intermediate" time, when the count rate was 1–5 counts s^{-1}; and (3) "faint" time, when the count rate was below <1 count s^{-1}. These three time intervals covered 60 s, 113 s, and 12.15 ks of exposure, respectively. For each time interval an X-ray image was formed, and a radial profile was calculated by binning the counts in 2 pixel wide annuli centered on the source (taken to be at the centroid of the faint image).

The three radial profiles were compared to a model comprising an analytical PSF model and a constant background (per pixel) using XSPEC, version 11.3. Both the PSF and background models were integrated in annuli to compare with the measured radial profiles:

$$M(r_{\rm in}, r_{\rm out}) = \int_{r_{\rm in}}^{r_{\rm out}} \left\{ N \left[1 + \left(\frac{r}{r_c} \right)^2 \right]^{-\beta/2} + B \right\} 2\pi r \, dr, \quad (1)$$
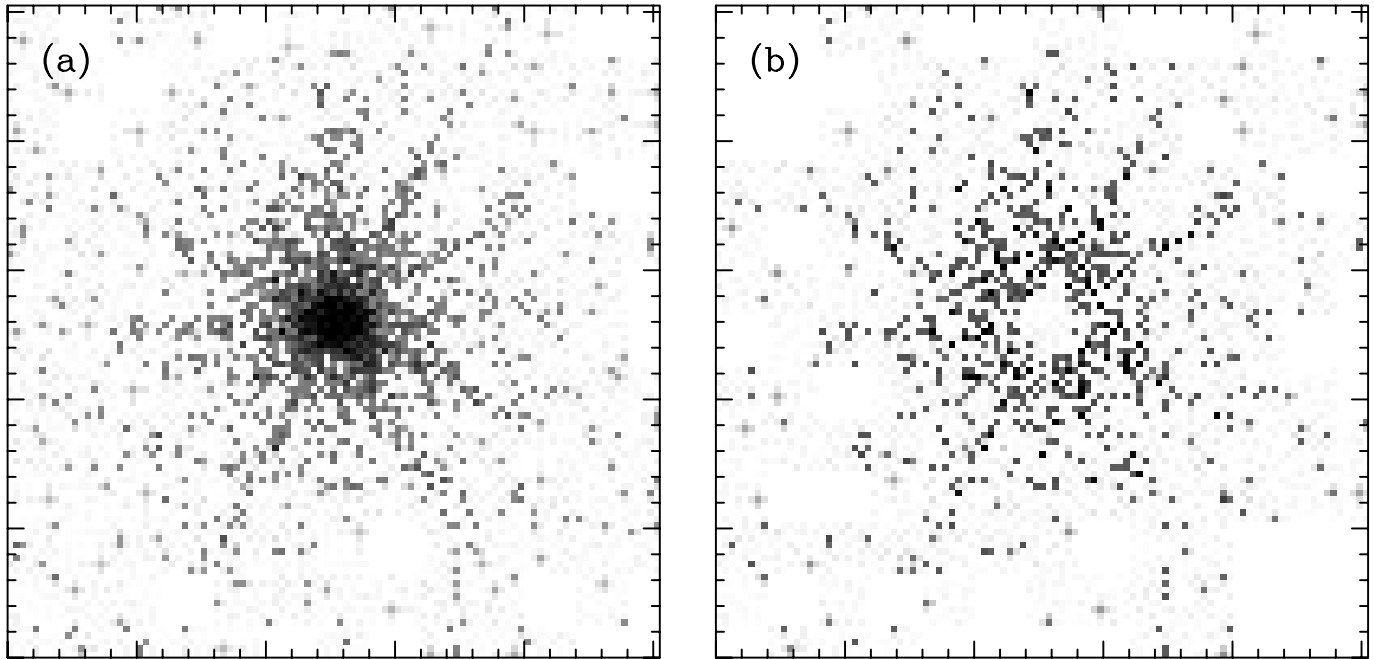
FIG. 2.—XRT images of GRB 050315 in the 0.2–5 keV range shown in detector coordinates. Panel (*a*) shows the events accumulated from the first 10 orbits of pointed exposures; the image is 100 pixels on a side (corresponding to 3′9). Panel (*b*) shows the image from only the first 60 s of exposure, when the source was brighter than >5 counts s^{-1}, clearly showing a "hole" in the center of the image caused by pileup.

where the first term in curly braces represents the King profile PSF, with parameters r_c and β, and the second term the constant background level, *B*. The PSF parameters were taken to be the same as used in § 3.4.

This model, with two free parameters (PSF normalization *N* and background level *B*), was fitted to the radial profile (counts per annulus) by adjusting the parameters to minimize the *C*-statistic (Cash 1979), which is equivalent to finding the maximum likelihood (ML) parameters from Poisson distributed data. The *C*-statistic was used as the fit statistic, instead of the more common χ^2, because only the former gives the ML parameters when there are few counts per bin, as was the case here. The disadvantage of using the *C*-statistic is that is does not directly provide a goodness-of-fit measure, but this can be obtained through Monte Carlo simulations. For each model 10^4 simulated profiles were generated, drawing each datum from the appropriate Poisson distribution, and the number of simulated data with a lower *C*-statistic (i.e., a better fit to the data) was used as a measure of the rejection probability *p*. The analytical PSF model provided a good fit to the faint radial profile, with $p = 0.50$, confirming that this model is indeed a good description of the source image at faint fluxes. The measured and fitted profiles are shown in Figure 3.

The same model was then fitted to the radial profiles from the intermediate and bright images but gave an unacceptable fit to the data, with $p > 0.9999$ in both cases, entirely due to the loss of counts in the center of the image. Severe pileup will produce a deficit of events in the central parts of the image, but the wings of the PSF should be relatively unaffected. Beyond some radius from the center the observed image should be consistent with the PSF model; this radius was estimated by excluding the innermost annuli from the radial profiles until the fit became acceptable ($p < 0.90$). In the case of the intermediate image (1–5 counts s^{-1}) excluding the innermost 8 pixel radius (19″) gave a good fit ($p = 0.797$), while for the bright image (>5 counts s^{-1}) the innermost 14 pixels (33″0) had to be excluded before the fit became acceptable ($p = 0.863$).
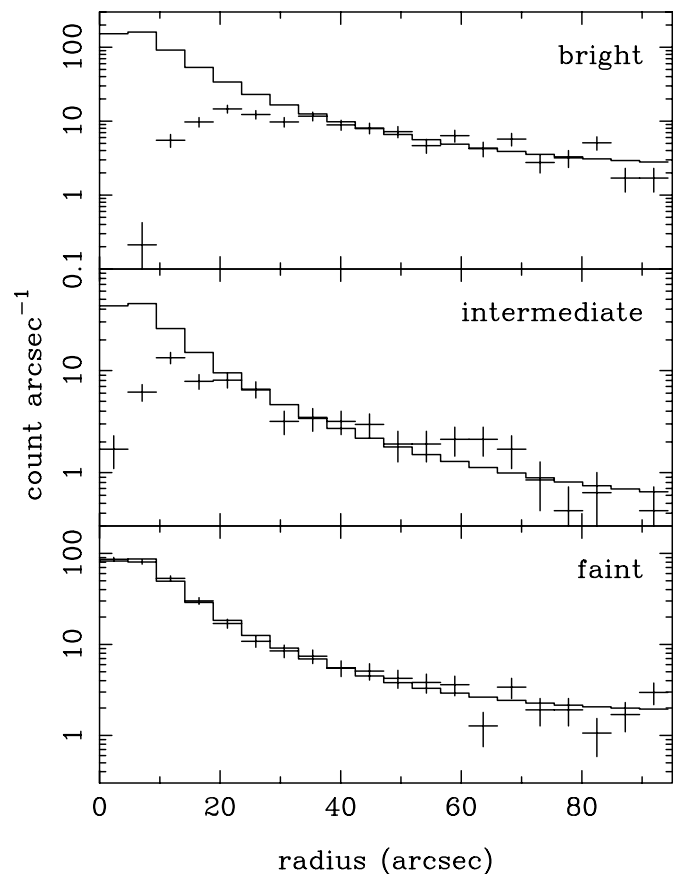

FIG. 3.—Radial profiles produced by integrating the counts in 2 pixel wide annuli centered on the source centroid. The three profiles were extracted from times when the source was bright (>5 counts s^{-1}), intermediate (1–5 counts s^{-1}), and faint (<1 count s^{-1}). The data are shown with plus signs, and the histogram shows the model (PSF + background) that provided a good fit to the wings of the PSF (see text for discussion). Clearly, when the source was faint the PSF model gave an accurate description of the radial profile, but when the source was brighter there was a substantial loss of counts at small radii.
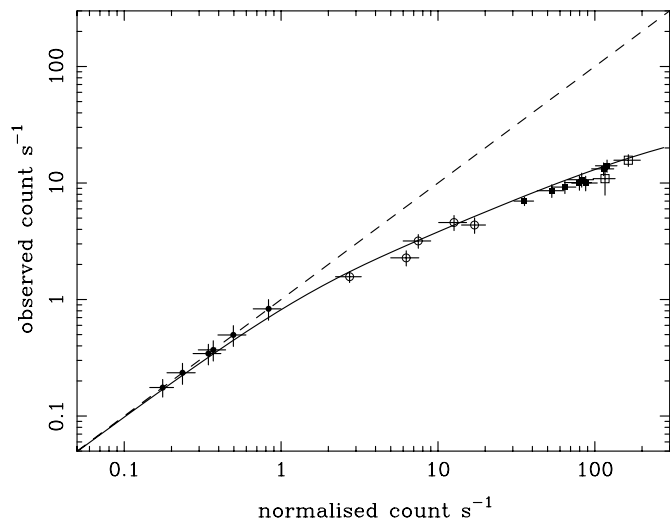
Fig. 4.—Count rate losses due to pileup. The abscissa represents the pileup-corrected count rate (i.e., after excluding the central part of the PSF and renormalizing to correct for the losses), which should be comparable to the true input source count rate. The ordinate represents the observed count rate extracted from a simple circular extraction region (i.e., without taking any account of pileup). The open squares indicate the settling data, the filled squares the bright data, the open circles the intermediate data, and the filled circles the faint data (the latter were not corrected for pileup). The dashed curve marks the expectation in the limit of no pileup. The solid curve marks the theoretically predicted relation between monopixel event count rates with and without pileup effects, based on eq. (6) of Ballet (1999). [*See the electronic edition of the Journal for a color version of this figure.*]

As a final check for the effects due to pileup at different fluxes, the data were divided into finer flux intervals. Radial profiles were extracted from times when the source was brighter than 10 counts s^{-1} and between 0.2 and 1.0 counts s^{-1}. These were fitted with the PSF model as above. For the very brightest data, excluding the central 14 pixels again provided an acceptable fit to the data ($p = 0.635$), whereas excluding only the inner 12 pixels did not ($p = 0.969$). These results indicate that an inner radius cutoff of 14 pixels (i.e., including only data from $\geq$15 pixels away) is sufficient to exclude the piled-up region of the source image even at its brightest. Examining the image taken when the source count rate was 0.2–1.0 counts s^{-1}, the PSF model gave a good fit down to the innermost pixel, confirming that pileup is a weak effect at $\lesssim$1 count s^{-1} ($\lesssim$20% flux loss; see Table 1).

On the basis of the above analysis, the following "work-around" procedure was used to mitigate the adverse effects of pileup. Source events were extracted from a circular region of 60″ (25 pixels) radius, excluding the center of the region when the source was bright. In particular, for the period until 146 s after the burst trigger, when the observed source count rate persistently exceeded 5 counts s^{-1}, an annulus with inner and outer radii of 15 and 25 pixels was used for the extraction region. Data from the period from 146 to 259 s, during which the source count rate was 1–5 counts s^{-1}, were extracted between radii of 9 and 25 pixels. All data taken at later times, when the source flux was below ~1 count s^{-1}, were extracted using a full circular region. Data extracted from annular regions were renormalized to account for the loss of the central part of the PSF. The correction factors, calculated by integrating the King PSF model,[16] were

---

[16] These correction factors were checked against those calculated using two alternative methods. The first used the function of the encircled energy, derived from ground calibration data and stored in the swxeef20010101v001.fits file in the *Swift* CALDB. The second folded a $\Gamma = 2$ power-law spectrum through the response matrices generated for the appropriate source extraction regions. In all cases the factors were very similar.
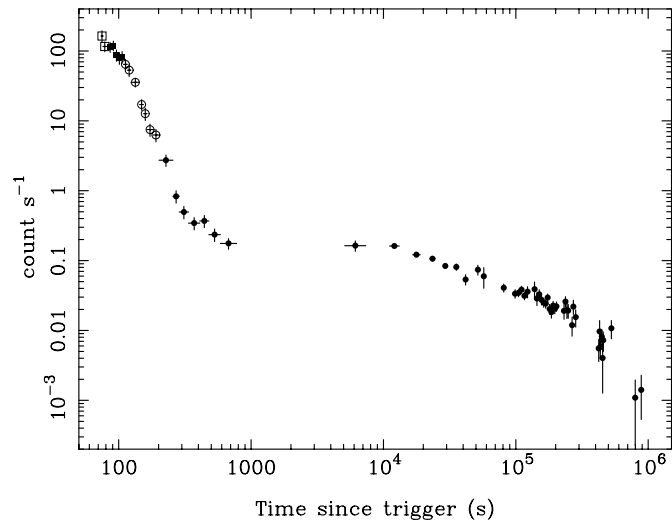

Fig. 5.—Light curve of GRB 050315 in the 0.2–5 keV band. These data have been corrected for pileup; the different symbols reflect the different corrections. The symbols have the same meaning as in Fig. 4. Times are in the observed frame (i.e., not corrected for cosmological time dilation).

14.4 and 5.0 for the data extracted during bright and intermediate fluxes, respectively.

The overall effect of pileup can be seen by comparing the light curve extracted from the first orbit of data before and after pileup correction. Figure 4 shows the relationship between the corrected and uncorrected count rates, which indicates the effect of pileup as a function of source intensity. Also shown is the theoretical curve derived from equation (6) of Ballet (1999), and discussed in § 3.1, for the relation between monopixel event count rates with and without pileup effects. Clearly the empirical correction of pileup matches the theoretical expectation based on the known CCD and PSF characteristics.

3.3. *Timing Analysis*

The 0.2–5 keV light curve of GRB 050315 was extracted from the full XRT data set. The first orbit, when the source was at its brightest, was treated separately to avoid pileup. The data were extracted in 2.507 s bins (i.e., one CCD frame) and then rebinned such that each time bin contained $\geq$25 events. (This permits the use of χ^2 minimization as a ML method.) Error bars were calculated using counting statistics. The three different time intervals during which the source was bright, intermediate, and faint were extracted using the different regions, to account for different degrees of pileup, as discussed above. A background light curve was extracted from an annulus centered on the source with inner and outer radii of 60 and 120 pixels (141″ and 283″), respectively, and subtracted from the source light curve. The three light curves from the different brightness intervals were renormalized to account for PSF losses; the resulting pileup-corrected light curve is shown in Figure 5. Also included in this figure are the data taken from the settling phase (see § 2.2), treated for pileup in the same fashion as the bright data.

The other orbits, for which pileup is not an issue, were extracted in the standard fashion, using a 60″ circular source region and the same background region as for the first orbit. These data were binned to produce one bin per orbit, accepting only those orbits containing at least 15 counts within the source region. The light curve spanning all XRT observations of GRB 050315 is shown in Figure 5.

The light curve was parameterized by fitting simple analytical models, comprising connected power laws [e.g., $F(t) \propto (t - T_0)^{-\alpha}$], using XSPEC to minimize the χ^2 fit statistic. Initially, the

TABLE 2
RESULTS OF XRT LIGHT-CURVE FITTING

Orbits	α	t_{br} (s)	α	t_{br} (s)	α
1..........	1.8 ± 0.9	115 ± 12	$5.2^{+0.5}_{-0.4}$	308^{+38}_{-33}	1.2 ± 0.6
2+	<0.41	$1.2^{+0.5}_{-0.3} \times 10^4$	0.71 ± 0.04	$2.5^{+1.1}_{-0.3} \times 10^5$	$2.0^{+1.7}_{-0.3}$
All	$1.9^{+0.7}_{-1.0}$	118 ± 12	$5.3^{+0.5}_{-0.4}$	...	...
	$0.06^{+0.08}_{-0.13}$	$1.2 \pm 0.4 \times 10^4$	0.71 ± 0.04	$2.5^{+1.1}_{-0.3} \times 10^5$	$2.0^{+1.7}_{-0.3}$

NOTES.—The models fitted to the first orbit (76–778 s postburst) and later orbits (5×10^3–9×10^5 s) were doubly broken power laws, with slopes and break times as stated. The model fitted to all data was the sum of a singly broken power law and a doubly broken power law.

first orbit (76–778 s postburst) and later orbits (5×10^3–9×10^5 s) were treated separately, before fitting the entire light curve. Through this section, and the rest of the paper, uncertainties on fitted parameters correspond to $\Delta\chi^2 = 2.706$ (i.e., a nominal 90% confidence region), unless stated otherwise.

A power law with no breaks or just one break did not fit the first orbit data (rejection probability $p > 0.9999$), whereas a doubly broken power law gave a very good fit ($\chi^2 = 6.90$ with 15 dof and $p = 0.04$). (Even after discounting the two time bins from the settling data, the improvement between the singly broken and doubly broken power law is significant at 99.4% confidence using an F-test.) The light curve for the first 700 s is strongly curved on a $\log(F_X)$–$\log(t - T_0)$ plot (Fig. 5), progressing through flat then steep then flat phases. The best-fitting parameters for the doubly broken power-law model are given in the first row of Table 2. The initial steepening of the decay during the first $\approx$200 s is reminiscent of an exponential decay, as observed in the prompt BAT light curve (§ 2.1). This possibility is discussed further below.

The later orbit light curve was also inconsistent with a power law ($p > 0.9999$), but a singly broken power law provided a good fit ($\chi^2 = 38.86$ with 39 dof and $p = 0.52$). However, including a second break improved the fit substantially ($\chi^2 = 28.63$ with 37 dof and $p = 0.16$). This improvement is significant at 99.6% confidence, using the F-test. A smooth bend from one power-law index to another gave a much worse fit that two sharp breaks. The late-time data therefore also show two break times (as given in the second row of Table 2). Thus, the complete XRT light curve for GRB 050315 shows at least four breaks if interpreted as a series of connected power laws. In fact, the complete light curve is well fitted by the sum of two components, a singly broken power law dominating before $\sim T_0 + 300$ s and a doubly broken power law dominating afterward ($\chi^2 = 38.77$ for 54 dof; $p = 0.06$). The best-fitting parameters for this model are shown in Table 2 (rows [3] and [4]), and the model is shown in Figure 6.

The only way to reconcile the early (flat-steep) part of the light curve with a single (unbroken) power law is by allowing the start time to be 165 ± 11 s prior to the BAT trigger, which lies well before the precursor in the BAT light curve (see Fig. 1), in which case the early decay slope is $\alpha = 8.9^{+0.1}_{-1.5}$. This model gave an acceptable fit, but not as good as the model with a break at $T_0 + 120$ s ($\chi^2 = 54.46$ for 55 dof; $p = 0.47$).

Fitting the steep, early light curve with an exponential decay (plus the doubly broken power-law component to fit the later time data) also gave a good fit, with $t_e = 35 \pm 2$ s, although not as good as the broken power law ($\chi^2 = 47.76$ for 56 dof, $p = 0.23$). Extrapolating the exponential (prompt) plus broken power-law (afterglow) model between 10^{-2} and 10^7 s, the total luminos-
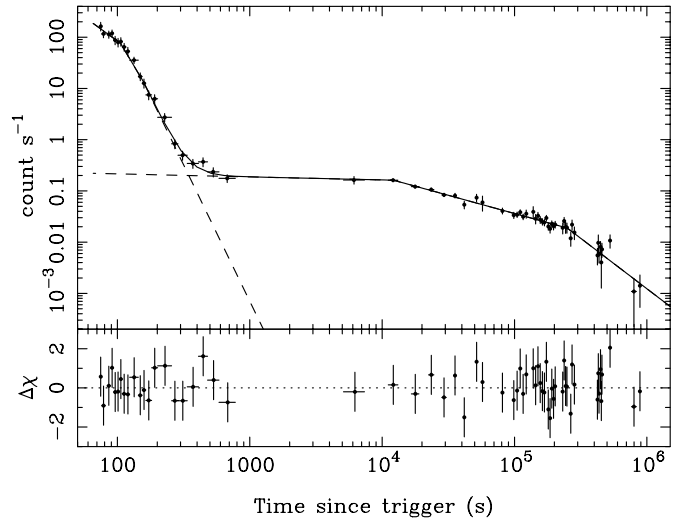

FIG. 6.—Light curve of GRB 050315 in the 0.2–5 keV band, as in Fig. 5, also showing the best-fitting model comprising a singly broken power law and a doubly broken power law, which dominate at early and late times, respectively (see Table 2). The lower panel shows the (data − model)/σ residuals. [*See the electronic edition of the Journal for a color version of this figure.*]

ity in the late-time broken power-law component is $\sim$32% of that in the "prompt" exponentially decaying component (assuming no spectral evolution).

3.4. *Spectral Analysis*

XRT spectra were extracted from monopixel events collected from source and background regions and grouped such that the source spectrum contained at least 20 counts per bin. (Fitting the raw, ungrouped data using the C-statistic did not alter the main results.) Five spectra were extracted from the following time intervals. From the first pointing there were three intervals: bright, intermediate, and faint as discussed above. One spectrum was extracted from the second pointing, which lasted from 0.69×10^5 to 2.4×10^5 s postburst (with an exposure time of 40.5 ks). This is referred to as the "mid" spectrum and lies on the $\alpha \approx 0.7$ part of the decay light curve. The fifth spectrum was extracted
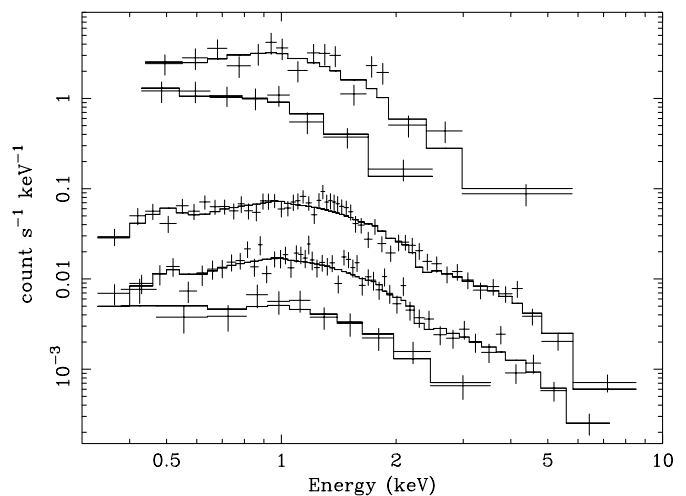

FIG. 7.—XRT spectra of GRB 050315. From the top down these correspond to the following time intervals: 86–146 s (bright), 146–259 s (intermediate), 259 s–57.39 ks (faint), $(0.69-2.4) \times 10^5$ s (mid), and $(2.7-5.3) \times 10^5$ s (late). The data are shown with plus signs, and the best-fitting absorbed power-law model in each case (see Table 3) is shown as a histogram

TABLE 3
RESULTS OF BAT AND XRT SPECTRAL FITTING

Data	Time ($+T_0$ s)	Γ	N_H	χ^2	dof	p
BAT peak.........	25.6–26.6	2.3 ± 0.2	...	51.79	56	0.37
BAT T_{50}............	0.0–24.7	2.02 ± 0.07	...	56.11	56	0.53
BAT T_{90}............	−48 to 48	2.13 ± 0.07	...	51.43	56	0.35
BAT total..........	−56 to 69	2.16 ± 0.07	...	55.34	56	0.50
XRT bright.......	76–146	2.5 ± 0.4	1.2 ± 0.7	21.01	14	0.90
XRT inter	146–259	$2.9^{+1.0}_{-0.8}$	<2.1	2.07	5	0.16
XRT faint........	$259–5.7 \times 10^4$	1.73 ± 0.11	0.5 ± 0.2	57.76	51	0.76
XRT mid..........	$0.69–2.4 \times 10^5$	1.79 ± 0.13	0.8 ± 0.3	48.98	50	0.49
XRT late...........	$2.7–5.3 \times 10^5$	$1.7^{+0.5}_{-0.3}$	<1.0	5.0	8	0.24
BAT + XRT	...	2.18 ± 0.07	0.6 ± 0.4	79.65	71	0.76

NOTE.—N_H is in units of 10^{22} cm^{-2} at $z = 1.949$.

from the fourth pointing, which lasted from 2.7×10^5 to 5.3×10^5 s postburst (with an exposure time of 18.7 ks). This is referred to as the "late" spectrum and lies on the $\alpha \approx 2.0$ part of the decay light curve. (The third, fifth, and later pointings only provided <100 source counts and so were not used in the spectral analysis.) The data were corrected for pileup by extracting source counts from annuli with radii of 15–25 and 9–25 (inclusive) pixels during the bright and intermediate time intervals, as for the light curve, and using an appropriate ancillary response file to correct for the PSF losses.

These spectra were fitted with absorbed power-law models. The Galactic column in the direction of GRB 050315 is $N_H = 4.3 \times 10^{20}$ cm^{-2} (Dickey & Lockman 1990), and this was kept fixed, using the TBabs model of Wilms et al. (2000). A second neutral absorber in the GRB frame (i.e., $z = 1.949$) was included to model any intrinsic absorption. The five XRT spectra are shown in Figure 7. In all cases a power law with excess absorption provided a good fit to the data. The results for the XRT spectral fitting are shown in Table 3, along with the results of fitting the BAT spectra. There is evidence that the spectrum softened between the bright spectrum (i.e., $< T_0 + 146$ s) and the faint spectra (i.e.,

FIG. 9.—Spectra from the BAT (on the right) from $T_0 − 56$ to $T_0 + 69$ s and bright XRT data (on the left) from $T_0 + 76$ to $T_0 + 146$ s, fitted simultaneously with a single absorbed power law ($\Gamma = 2.15 \pm 0.07$). [*See the electronic edition of the Journal for a color version of this figure.*]

$> T_0 + 259$ s), but the absorption columns remain consistent within the errors. This is illustrated by Figure 8, which shows the $\Delta\chi^2$ contours for the slope and column derived from the bright and faint data.

4. BAT-XRT COMPARISON

The early (bright) XRT spectrum (§ 3.4) showed a power-law slope not dissimilar to that of the BAT spectrum (§ 2.1). As a test of whether the early X-ray emission was connected to the prompt γ-ray emission, the BAT and early XRT spectra were fitted simultaneously. Figure 9 shows the XRT spectrum from the bright data ($\approx 86–146$ s posttrigger) and the BAT spectrum (extracted from the full time interval) fitted with the same absorbed power-law model, but with different normalizations between the two spectra (which allows for the temporal decay between the times of the BAT and early XRT observations). A single absorbed power law gave a good fit to the combined data (see Table 3), consistent with the hypothesis that the early X-ray emission and prompt hard
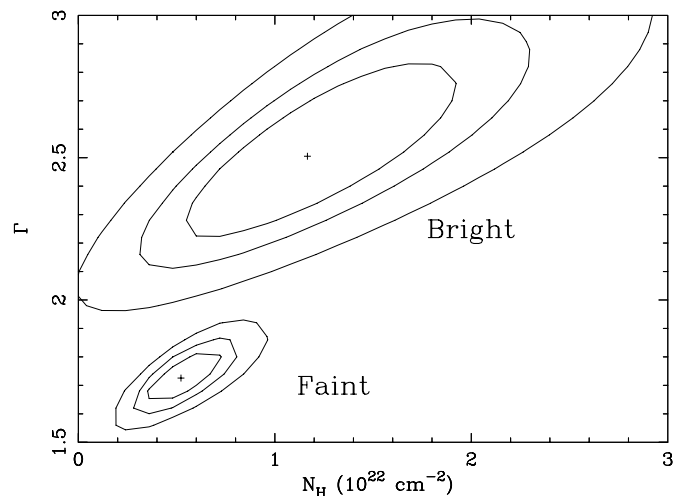

FIG. 8.—Confidence contours for spectral model parameters (excess absorption column and photon index) as fitted to the bright (86–146 s) and faint (259 s–57.39 ks) XRT data. The lines shown are the $\Delta\chi^2 = 2.30$, 4.61, and 9.21 contours (nominal 68.3%, 90%, and 99% confidence bounds). The photon index clearly decreased between bright and faint spectra. (The contours for the mid and later data are not shown but do overlap with those for the faint data.)
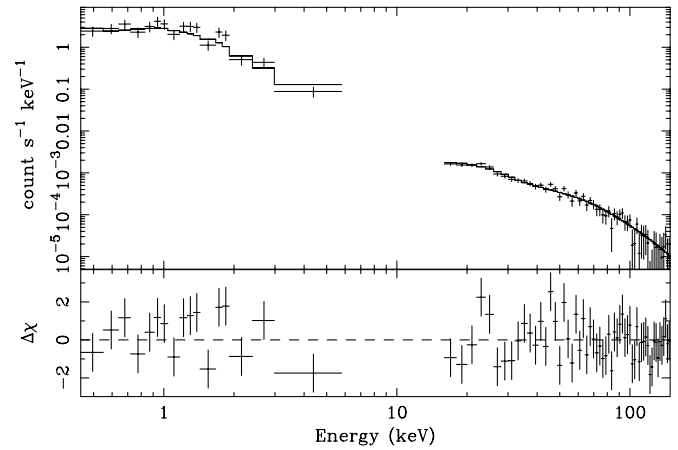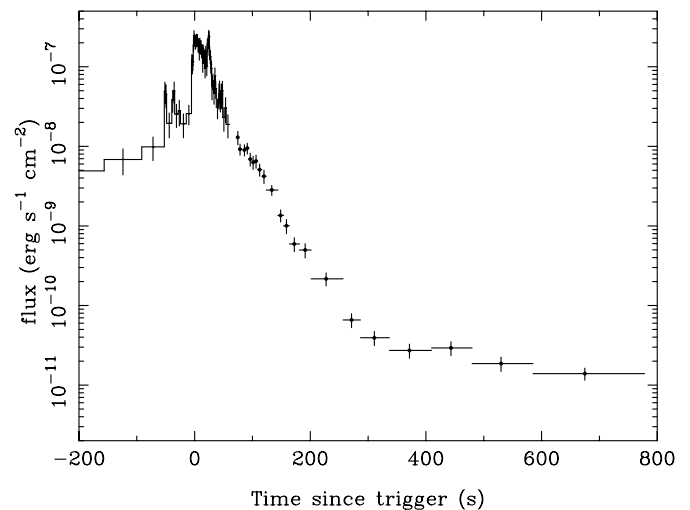

FIG. 10.—Light curves from the BAT (*histogram*) and first orbit of XRT data (*plus signs*) plotted in units of (unabsorbed) flux in the 0.2–10.0 keV band. The hard X-ray BAT light curve was extrapolated into the XRT energy band using the spectral fit discussed in § 4. [*See the electronic edition of the Journal for a color version of this figure.*]

X-ray/γ-ray emission were produced by the same emission spectrum.

The spectral fits to the BAT and XRT data were used to calculate the conversion between the observed count rate and the unabsorbed 0.2–10.0 keV flux for both BAT and XRT. The extrapolation of the BAT spectrum into the XRT bandpass should be reasonably accurate, since, as shown above, the prompt spectrum does extend, unbroken, into the XRT bandpass. These factors were then used to plot the XRT and BAT light curves in flux units, for comparison with one another. The error on the BAT flux resulting from the uncertainty in the spectral model was propagated into the 0.2–10.0 keV band and added in quadrature with the statistical error. The result is shown in Figure 10. From this figure it is clear that the tail end of the prompt emission seen by the BAT lies very close to the early XRT data, strongly supporting the idea that the early X-ray emission is an extension of the fading prompt emission. The combined BAT-XRT light curve is dominated by an approximately exponential decay in flux. (The agreement between BAT and XRT light curves does not depend on whether absorbed or unabsorbed fluxes are plotted.)

5. DISCUSSION

5.1. *Summary of Results*

The following are the main results of the XRT and BAT temporal and spectral analyses of the *Swift* observations of GRB 050315.

1. The BAT light curve showed two FRED-like peaks. The main peak fell away exponentially with a decay constant of $\approx 24 \pm 2$ s in the observer's frame ($t_e = 8 \pm 1$ s in the source frame). See Figure 1.

2. After correcting for pileup, the XRT light curve starting at $T_0 + 76$ s showed a very rapid decline (as steep as $\alpha \gtrsim 5$) until $\approx T_0 + 300$ s. The e-folding time during this period was 35 ± 2 s in the observer's frame (12 ± 1 s in the source frame). See Figures 5 and 6.

3. Despite modest spectral evolution in the BAT data, the BAT and early ($\lesssim T_0 + 150$ s) XRT spectra were both consistent with steep power laws ($\Gamma \approx 2.2$). See Figure 9.

4. Extrapolating the BAT light curve into the XRT energy band (using the best-fitting XRT + BAT spectral model) showed the early X-ray data to be consistent with the tail end of the exponentially decaying prompt emission. See Figure 10.

5. The XRT spectra show significant excess absorption in the rest frame of GRB 050315 ($N_H \sim 10^{22}$ cm^{-2}) with significant spectral hardening between early ($\lesssim T_0 + 150$ s) and later ($\gtrsim T_0 + 250$ s) times. See Figures 7 and 8.

6. After $T_0 + 300$ s, the X-ray flux decays only very slowly but shows further temporal breaks at $(1.2 \pm 0.4) \times 10^4$ s $[(4.1 \pm 1) \times 10^3$ s source frame] to a slope of $\alpha \approx 0.7$ and again at $2.5^{+1.1}_{-0.3} \times 10^5$ s ($8^{+3}_{-1} \times 10^4$ s source frame) to a steeper slope of $2.0^{+1.7}_{-0.3}$. See Figures 5 and 6.

5.2. *Prompt Hard X-Rays/γ-Rays from GRB 050315*

GRB 050315 shows a relatively soft (steep) spectrum in both the BAT and early XRT data ($\Gamma \approx 2.2$). This has at least two interesting implications. The first is that GRB 050315 may be classified as an "X-ray–rich" GRB or an "X-ray flash" (XRF). These classifications are often made using the softness ratio SR = log $[S_X(2-30 \text{ keV})/S_\gamma(30-400 \text{ keV})]$ (Lamb et al. 2004; Sakamoto et al. 2004), with $-0.5 <$ SR < 0 for an X-ray–rich burst and SR > 0 for an XRF. The joint BAT-XRT spectral fit (§ 4) gave SR = 0.2, suggesting that GRB 050315 may be better classified as an XRF.

The second implication of the soft spectrum is that the energy at which the emission peaks (the peak in E-F_E space) is below the observed BAT energy range. This does not match the expectations of the E_{peak}-E_{iso} relation discovered by Amati et al. (2002). These authors showed that the peak energy and isotropic energy were correlated for a small sample of GRBs with known redshifts detected by *BeppoSAX*. Ghirlanda et al. (2005) found the same relation in Burst and Transient Source Experiment (BATSE) data. Using the E_{peak}-E_{iso} relation from Ghirlanda et al. (2005; their eq. [1]), the predicted peak energy for GRB 050315 is $E_{peak} \sim 163$ keV in the source frame, or ~ 55 keV in the observed frame, yet the observed BAT spectrum was an unbroken power law with $\Gamma \approx 2.2$ down to ~ 15 keV, suggesting a much lower E_{peak}. As shown in § 2.1, the peak energy (in the observer's frame) was constrained to $E_{peak} \lesssim 30$ keV (90% CL), which is at odds with the prediction of the Amati relation. Furthermore, the estimated E_{iso} is really a lower limit, since it was calculated over only 15–150 keV, meaning the predicted E_{peak} is a lower limit. If the true E_{iso} is higher, the predicted E_{peak} is also higher, and discrepancy with the Amati relation becomes even more severe.

5.3. *Prompt-Afterglow Transition in X-Rays*

The similarity of the spectral slopes from the early XRT data and the prompt BAT observation (Fig. 9) raises the interesting possibility that the prompt hard X-rays and early soft X-rays do not come from distinct components ("burst" and "afterglow") but are actually different parts of the same spectrum. The early soft X-rays may simply be the lower energy emission from the same component as the prompt hard X-ray/γ-ray emission that triggered the BAT. That the predicted soft X-ray flux from the BAT data matches the observed flux at the start of the XRT observation (Fig. 10) strongly supports this idea; furthermore, both the prompt hard X-rays and early soft X-rays decay in an approximately exponential fashion with similar e-folding timescales. Small differences in fluxes and decay timescales between the two bands are perhaps not surprising given that the spectrum of the prompt emission does evolve slightly (gets softer) with time. For example, if the X-ray flux is given by $F(t) \propto E^{-\beta(t)} \exp{(-t/t_e)}$, where $\beta = \Gamma - 1$ and $\beta(t)$ increases slightly with time, the softer X-rays would decay slightly slower, as observed.

If the X-ray emission before $\sim T_0 + 300$ s (100 s in the source frame) is dominated by the decay of the prompt burst spectrum, the subsequent emission may be identified with the more standard X-ray afterglow (Costa et al. 1997), which must have begun as the prompt emission decayed. The change in the X-ray spectrum after $\sim T_0 + 300$ s (see Fig. 8) supports the idea that these two time intervals should be considered as distinct phases. In the following discussion the emission before and after $\sim T_0 + 300$ s will be referred to as "prompt" and "afterglow," respectively. In the standard relativistic fireball models (e.g., van Paradijs et al. 2000; Mészáros 2002; Piran 2005), the prompt emission is caused by internal shocks within the expanding fireball, and the afterglow is the result of the external shocks, as the relativistic matter collides with circumburst material. The X-ray to γ-ray emission observed before $T_0 + 300$ s, with a spectral slope $\Gamma \approx 2.2$, is therefore identified with internal shocks, and the emission observed afterward, with a spectral slope $\Gamma \approx 1.8$, is identified with the external shocks.

Some other *Swift* bursts do not show such a strong connection between the BAT and XRT data, e.g., GRB 050219a (Tagliaferri et al. 2005). But the results for GRB 050315 are not completely without precedent. Tagliaferri et al. (2005) also reported the *Swift* observations of GRB 050126, with a simple FRED-like burst profile. When extrapolated into the XRT energy range, the predicted

flux at the end of the BAT light curve is of the same order as the observed flux in the early (from $\sim T_0 + 100$ s) XRT light curve. However, in this case, the prompt BAT spectrum was considerably harder than the early XRT spectrum. More convincing was GRB 050319 (Cusumano et al. 2006; Barthelmy et al. 2005b), for which the spectra from the prompt BAT and early XRT data were consistent, and the X-ray light curve was consistent with a single rapid decay from prompt emission, until overtaken by a more slowly fading X-ray afterglow at $\sim T_0 + 400$ s, which showed a harder X-ray spectrum. GRB 050117 (Hill et al. 2006) also showed reasonable agreement between the predicted X-ray flux from the BAT and the earliest X-ray flux measured by the XRT, despite the complex burst profile.

Several other *Swift* XRT observations of GRBs have revealed very rapid X-ray decays in the first few hundred seconds after the bursts (Hill et al. 2006; Tagliaferri et al. 2005). These may also be caused by the fading prompt source, perhaps off-axis emission (Kumar & Panaitescu 2000), in which case the mismatches between BAT and XRT light curves require explanation. It is conceivable that this is due to dramatic spectral evolution. After the first few 10^2 s, the X-ray emission is dominated by the afterglow, which stayed relatively constant before decaying as a broken power law.

5.4. The X-Ray "Plateau" Phase

From ≈ 300 s until $\approx 1.2 \times 10^4$ s (100–4×10^3 s in the source frame) the X-ray afterglow emission was almost perfectly constant $[\alpha_0 = 0.06^{+0.08}_{-0.13}$; using the convention that $F(\nu, t) \propto t^{-\alpha} \nu^{-\beta}$, where $\beta = \Gamma - 1]$, beyond which it broke to a power-law decay with a slope of $\alpha_1 = 0.7$. Such a flat afterglow light curve is unusual and has not been seen in other *Swift* bursts to date, although several other bursts have shown less extreme steep-flat-steep light curves (e.g., Chincarini et al. 2005; Hill et al. 2006). It must be said, however, that the sampling during this period is rather sparse, and it remains possible, although perhaps unlikely, that an X-ray rebrightening episode, such as observed in GRB 050406 and GRB 050502b (Burrows et al. 2005b), could have occurred during the gaps in the light curve, masking an underlying shallow decay.

The indices of the temporal decay and energy spectrum of the afterglow, α and β, respectively, are governed by the power-law index of the energy distribution of the electrons in the flow, p. The X-ray spectrum during the plateau phase (faint and mid spectra; Table 3) shows an energy index of $\beta \sim 0.7$. This rules out the X-ray band lying on the $\beta = -1/3$ part of the synchrotron spectrum, below the emission frequency of the lowest Lorentz factor electrons in the shock, ν_m, and the synchrotron cooling frequency, ν_c (e.g., Sari et al. 1998). However, this spectral index is close to the $\beta \sim 0.5$ expected if the X-ray band lies above ν_c but below ν_m. In this case the flux is expected to decay with $\alpha = 1/4$, which is steeper than the observed plateau phase ($\alpha \approx 0$), but a flatter decay could occur if inverse Compton scattering makes a significant contribution to electron cooling. This might be expected for the first few hours of a typical burst. After ν_m moves below the X-ray band (which occurs as $\nu_m \propto t^{-3/2}$), the expected decay steepens to $\alpha = (3p - 2)/4$, and thus a slope of $\alpha \approx 0.7$ predicts $p \approx 1.6$. Such a low p-value is unusual, but not totally without precedent (e.g., GRB 010222; Masetti et al. 2001). Thus, the break from $\alpha \approx 0$ to 0.7, marking the end of the plateau phase, could be due to ν_m moving below the X-ray band (in the standard forward shock model it is difficult to have ν_m much above the XRT band after 300 s).

Alternatively, the plateau phase of the light curve may be a consequence of "refreshed" shocks, i.e., energy is pumped into

the shock as it occurs. There are two simple scenarios that will result in refreshed shocks. The first is that there is a distribution of Lorentz factors in the jet such that slower material is continuously catching up with faster ejecta as it decelerates in the shock (e.g., Rees & Mészáros 1998; Sari & Mészáros 2000). The second scenario occurs when the central engine stays active for a prolonged period and continuously injects energy into the jet at a decreasing rate (e.g., Zhang & Mészáros 2001). After the energy injection ends (at ~ 12 ks), the flux would be expected to decay as a power law with an index $\alpha = 3(p - 1)/4$, provided that ν_c was above the XRT band. Using $p = 1 + 2\beta \approx 2.4$ gives $\alpha \approx 1.1$ for a uniform density interstellar medium, and steeper still for a medium consisting of the progenitor wind, inconsistent with the observations ($\alpha \approx 0.7$). If, on the other hand, ν_c was below the XRT band, then $p = 2\beta \approx 1.4$ and the flux decline is given by $\alpha = -(3p - 2)/4 = 0.55$, which is closer to the observed decline. This solution also requires $p < 2$.

5.5. Late-Time X-Ray Break

The X-ray afterglow shows a second break at 2.5×10^5 s (8.4×10^4 s in the source frame) to a much steeper decline, with $\alpha_2 = 2.0^{+1.7}_{-0.3}$. This might readily be identified with a "jet break," corresponding to the time when the beaming angle of the relativistic flow ($\theta_{\rm beam} \sim \gamma^{-1}$) becomes wider than its geometric opening angle (θ_0), after which the emission decays much faster (Sari et al. 1999; Rhoads 1999). Using equation (1) of Frail et al. (2001), the observed break timescale and $E_{\rm iso}$ yield a jet opening angle of $\theta_0 \sim 5°$, similar to the values derived for other bursts (Frail et al. 2001; Ghirlanda et al. 2005). The predicted "true" energy released in γ-rays, corrected for the small jet opening angle, is $E_\gamma = (1 - \cos\theta_0)E_{\rm iso} \gtrsim 1.2 \times 10^{50}$ ergs, somewhat below the mean energy found by Frail et al. (2001) or Bloom et al. (2003).[17] Of course, since the prompt spectrum from the BAT only covers the 15–150 keV range, then the total (bolometric) E_γ is probably a factor of a few larger, closer to the typical values.

If the X-rays are synchrotron emission above the cooling frequency ν_c, then the spectrum is expected to be $\beta = p/2$ (see Sari et al. 1999; Zhang & Mészáros 2004), which gives $p \approx 1.6$, matching the estimate above (§ 5.4) based on the temporal decay after the plateau. In this situation the predicted temporal slope after the jet break is $\alpha = p \approx 1.6$, which compares reasonably with the observed value of $2.0^{+1.7}_{-0.3}$. The jet break should be achromatic, and therefore the spectrum should remain unchanged across the jet break. Indeed, within the errors the spectral shapes are consistent before and after this break (the mid and late spectra of Table 3).

---

[17] GRB 050315 is not an "f-GRB," in the scheme of Bloom et al. (2003), because both the X-ray and R-band afterglow decays are very slow at $\approx T_0 + 0.5$ days.

REFERENCES

Amati, L., et al. 2002, A&A, 390, 81
Arnaud, K. 1996, in ASP Conf. Ser. 101, Astronomical Data Analysis Software and Systems V, ed. G. H. Jacoby & J. Barnes (San Francisco: ASP), 17
Ballet, J. 1999, A&AS, 135, 371
Band, D., et al. 1993, ApJ, 413, 281
Barthelmy, S. D. 2004, Proc. SPIE, 5165, 175
Barthelmy, S. D., et al. 2005a, Space Sci. Rev., 120, 143
———. 2005b, ApJ, 635, L133
Bersier, D., et al. 2005, GCN Circ. 3103, http://gcn.gsfc.nasa.gov/gcn/gcn3/3103.gcn3
Bloom, J. S., Frail, D. A., & Kulkarni, R. 2003, ApJ, 594, 674
Blustin, A. J., et al. 2006, ApJ, 637, 901
Burrows, D. N., et al. 2004, Proc. SPIE, 5165, 201
———. 2005a, Space Sci. Rev., 120, 165
———. 2005b, Science, 309, 1833
Cash, W. 1979, ApJ, 228, 939
Chincarini, G., et al. 2005, ApJ, submitted (astro-ph/0506453)
Cobb, B. E., & Bailyn, C. D. 2005, GCN Circ. 3104, http://gcn.gsfc.nasa.gov/gcn/gcn3/3104.gcn3
Costa, E., et al. 1997, Nature, 387, 783
Cusumano, G., et al. 2006, ApJ, 639, 316
De Pasquale, M., et al. 2006, MNRAS, 365, 1031
Dickey, J. M., & Lockman, J. 1990, ARA&A, 28, 215
Frail, D. A., et al. 2001, ApJ, 562, L55
Gehrels, N., et al. 2004, ApJ, 611, 1005
Ghirlanda, G., Ghisellini, G., & Firmani, C. 2005, MNRAS, 361, L10
Hill, J. E., et al. 2004, Proc. SPIE, 5165, 217
———. 2006, ApJ, in press (astro-ph/0510008)
Jakobsson, P., et al. 2006, A&A, in press (astro-ph/0509888)
Kelson, D., & Berger, E. 2005a, GCN Circ. 3100, http://gcn.gsfc.nasa.gov/gcn/gcn3/3100.gcn3
———. 2005b, GCN Circ. 3101, http://gcn.gsfc.nasa.gov/gcn/gcn3/3101.gcn3
Krimm, H., Parsons, A., & Markwardt, C. 2004, BAT Ground Analysis Software Manual, (Greenbelt: NASA), http://heasarc.gsfc.nasa.gov/docs/swift/analysis/BAT_GSW_Manual_v2.pdf

Krimm, H., et al. 2005, GCN Circ. 3105, http://gcn.gsfc.nasa.gov/gcn/gcn3/3105.gcn3
Kumar, P., & Panaitescu, A. 2000, ApJ, 541, L51
Lamb, D. Q., et al. 2004, NewA Rev., 48, 423
Masetti, N., et al. 2001, A&A, 374, 382
Mészáros, P. 2002, ARA&A, 40, 137
Moretti, A., et al. 2004, Proc. SPIE, 5165, 232
Morris, D. C., et al. 2005, GCN Circ. 3097, http://gcn.gsfc.nasa.gov/gcn/gcn3/3097.gcn3
Mukerjee, K., Abbey, A. F., Osborne, J. P., & Beardmore, P. 2003, University of Leicester Technical Report XRT-LUX-CAL-100 (Leicester: Univ. Leicester)
Nousek, J. A., et al. 2005, ApJ, submitted (astro-ph/0508332)
Parsons, A., et al. 2005, GCN Circ. 3094, http://gcn.gsfc.nasa.gov/gcn/gcn3/3094.gcn3
Piran, T. 2005, Rev. Mod. Phys., 76, 1143
Rees, M. J., & Mészáros, P. 1998, ApJ, 496, L1
Rhoads, J. E. 1999, ApJ, 525, 737
Roming, P. W. A., et al. 2005, Space Sci. Rev., 120, 95
Rosen, S., et al. 2005, GCN Circ. 3095, http://gcn.gsfc.nasa.gov/gcn/gcn3/3095.gcn3
Sakamoto, T., et al. 2004, ApJ, 602, 875
———. 2005, GCN Circ. 3099, http://gcn.gsfc.nasa.gov/gcn/gcn3/3099.gcn3
Sari, R., & Mészáros, P. 2000, ApJ, 535, L33
Sari, R., Piran, T., & Halpern, P. 1999, ApJ, 519, L17
Sari, R., Piran, T., & Narayan, R. 1998, ApJ, 497, L17
Soderberg, A. M., & Frail, A. 2005, GCN Circ. 3102, http://gcn.gsfc.nasa.gov/gcn/gcn3/3102.gcn3
Tagliaferri, G., et al. 2005, Nature, 436, 985
van Paradijs, J., Kouveliotou, C., & Wijers, J. 2000, ARA&A, 38, 379
Wilms, J., Allen, A., & McCray, R. 2000, ApJ, 542, 914
Zhang, B., & Mészáros, P. 2001, ApJ, 552, L35
———. 2004, Int. J. Mod. Phys., 19, 2385

Note added in proof.—A recent recalculation of the intrinsic scatter in the E_{peak}-E_{iso} correlation by L. Amati et al. (2005, private communication), estimating the scatter on E_{peak} at more than 0.4 dex, places GRB 050315 just within the acceptable range of this correlation. Confirmation of the intrinsic scatter in the correlation will clarify the situation.